

Design of wide-range energy material beamline at the Shanghai Synchrotron Radiation Facility

Zhen-Hua Chen¹ · Fan-Fei Sun¹ · Ying Zou¹ · Fei Song¹ · Shuo Zhang¹ · Zheng Jiang¹ · Yong Wang¹ · Ren-Zhong Tai¹

Received: 10 November 2016/Revised: 31 July 2017/Accepted: 8 August 2017/Published online: 5 February 2018
© Shanghai Institute of Applied Physics, Chinese Academy of Sciences, Chinese Nuclear Society, Science Press China and Springer Nature Singapore Pte Ltd. 2018

Abstract We report the design of a wide-range energy material beamline (E-line) with multiple experimental techniques at the Shanghai Synchrotron Radiation Facility. The undulators consisted of an elliptically polarizing undulator and in-vacuum undulator that generate the soft and hard X-rays, respectively. The beamline covered a wide energy range from 130 to 18 keV with both a high photon flux ($> 10^{12}$ phs/s with exit slit 30 μm in soft X-ray and $> 5 \times 10^{12}$ phs/s in hard X-ray within 0.1%BW bandwidth) and promising resolving power (maximum $E/\Delta E > 15,000$ in soft X-ray with exit slit 30 μm and > 6000 in hard X-ray). Moreover, the beam spots from the soft and hard X-rays were focused to the same sample position with a high overlap ratio, so that the surfaces, interfaces, and

bulk properties were characterized in situ by changing the probing depth.

Keywords Synchrotron radiation · Beamline · Wide energy range · E-line · Shanghai Synchrotron Radiation Facility

1 Introduction

Key scientific issues in energy demands rely on the development of material science. The in situ study at the atom/molecular basic level is critical in understanding the electronic structure and reaction mechanism, benefiting the synthesis of new energy materials, such as catalysis and batteries [1–8]. However, the existing “pressure gap” between the real complex environment and a model system characterized in vacuum or ultra-high vacuum conditions always leads to inaccurate experimental results [9, 10].

New characterization techniques are urgently needed to study these materials in the real environment. Due to the advantages of a high photon flux and spectral continuity, synchrotron radiation-based X-rays are employed as light sources for the spectroscopic and diffraction studies [11, 12]. Nevertheless, the currently running beamlines in most synchrotron radiation facilities cannot demonstrate comprehensive characterization for the material systems due to limited research methods. Additionally, the buried interfaces in energy materials, such as the solid–liquid interface in electrochemical batteries, multilayer light-emitting devices, thin-film photovoltaic cells, and complex catalysts, are difficult to characterize in situ because of the limited probing depth. Therefore, building a wide-energy-

Zhen-Hua Chen and Fan-Fei Sun have contributed equally to this work.

This work was supported by the National Development and Reform Commission (NDRC) of China, the National Natural Science Foundation of China (No. 11505280), the Shanghai Youth Foundation (No. 14YF1407500), and the National Science Foundation of China (Nos. 11475251, 11225527).

Electronic supplementary material The online version of this article (<https://doi.org/10.1007/s41365-018-0356-6>) contains supplementary material, which is available to authorized users.

✉ Ying Zou
zouying@sinap.ac.cn

✉ Zheng Jiang
jiangzheng@sinap.ac.cn

✉ Yong Wang
wangyong@sinap.ac.cn

¹ Shanghai Institute of Applied Physics, Chinese Academy of Sciences, Shanghai 201204, China

range experimental platform with multiple methods will greatly aid the research for these energy materials.

In this project, a wide-energy-range beamline with multiple analysis platforms was designed to conduct experiments for in situ conditions. Both the soft and hard X-ray branches were operated so that a broad penetration range could be achieved. Various depth of materials, including buried interfaces, were characterized by tuning the wavelength of the incident X-rays by referring to the “universal” curve between the electrons mean free path and their kinetic energy [13, 14].

The design presented here is unique and not found elsewhere in the literature; however, there is a partially completed project at the Diamond light source (I09) in the UK, and similar systems are planned to be built at NSLS-II (SST) in the USA and BESSY II (EMIL) in Germany [15–17]. Among these beamlines, the E-line in the SSRF covers the widest energy range (130–18 keV) with a comparable flux and energy resolution. The newly designed experimental platform in the SSRF based on such soft/hard X-ray combined beamlines has the following characteristics. First, by referring to the relationship between the photoelectron escape length and its kinetic energy, depth-resolved element analysis at the atomic layer level resolution and a comprehensive study of microstructures under in situ conditions were achieved. Second, multiple spectroscopic methods, including inelastic resonant X-ray emission spectroscopy (RXES), resonant elastic X-ray scattering (REXS), X-ray absorption spectroscopy (XAS), ambient pressure photoelectron spectroscopy (APPES), hard X-ray emission spectroscopy (HAXES), and hard X-ray Raman spectroscopy (XRS), were established to study the local structure of the complex molecules and spin structures in different constituents during the chemical reaction process. In accordance with these characteristics, the crucial areas of the directional catalysis, batteries, light-emitting devices, photovoltaic materials, electrochemical processes, corrosion, and surface protection were incorporated in this platform.

2 Undulator light source

The SSRF is composed of a 3.5 GeV electron storage ring, 3.5 GeV booster, and 150 MeV linac. The beam current in the storage ring is 250 mA. Two undulators, EPU and IVU, are located in the same straight line with a canted angle of 2 mrad. The EPU with a period length of 60 mm, 30 periods, and a maximum k -value of 5.3 was selected to cover the soft X-ray regime from 130 to 1500 eV, while the IVU with a period length of 24 mm, 65 periods, and a maximum k -value of 1.7 was used for the

hard X-ray regime from 1500 to 18 keV. The parameters of the EPU and IVU of the E-line are given in Table 1.

The calculated values for the photon flux within the acceptance angle of both undulators are shown in Fig. 1a. Both the horizontal and vertical divergence values varied dramatically in the soft X-ray range, necessitating variability in the aperture (white slit) with energy. In contrast, the divergence was marginal for the hard undulator (Fig. 1b). In this project, a 4σ aperture was adopted in the soft X-ray range (130–1500 eV), dependent on the incident photo energy, whereas a fixed 3σ ($113 \mu\text{rad} \times 53 \mu\text{rad}$) aperture was adopted in the hard X-ray (1500 eV–18 keV) to maximize and utilize the photons from the light source.

3 Beamline

3.1 Optical path design

The schematic beamline layout of the E-line is shown in Fig. 2. Two separated beamlines, corresponding to soft and hard X-rays, are sketched in red and blue, respectively, and were in close proximity to the APPES experimental end station. The soft X-ray branch passed through two series of experimental stations, REXS and inelastic RXES, while the hard X-ray branch was connected to a HAXES end station.

With the canted angle of 2 mrad, the two undulator beams propagate until their separation is large enough to mount a separate plane mirror, SM1, which is located at distances of 15.9 m relative to the center of straight section. This keeps the Bremsstrahlung radiation within the ring tunnel and eases the radiation safety measures in the experimental hall. After the first mirror, the angular separation of the two beams increases to 1.2° , allowing for the setup of two dedicated beamlines.

Although the main beam toward the HAXES station did not pass through SM1, Bremsstrahlung radiation was still generated from the scattering effect of SM1 and was

Table 1 Parameters of the EPU (soft X-ray) and IVU (hard X-ray) of the E-line in the SSRF

Parameters	EPU	IVU
Total length (m)	1.80	1.56
Energy range (eV)	130–1500 eV	1500–18,500
Periodic length (mm)	60	24
Number of periods	30	65
Maximum k -value	5.3	1.7
Peak magnetic fields (T)	0.907	0.96
Minimum gap (mm)	14.5	5

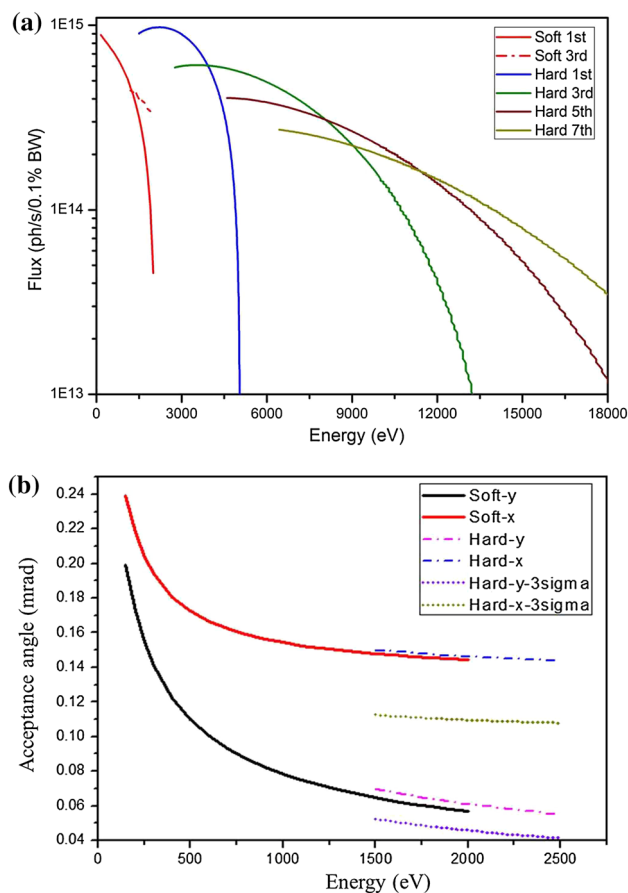


Fig. 1 (Color online) **a** The photo flux of the soft and hard X-ray undulators depend on the energy within the acceptance angle (simulated via the SPECTRA program [18]). A 4σ aperture was adopted in the soft X-ray range 130–1500 eV, dependent on the incident photo energy, whereas a fixed 3σ ($113 \mu\text{rad} \times 53 \mu\text{rad}$) aperture was adopted in the hard X-ray range 1500 eV–18 keV. The photon flux of the first (solid line) and third (dashed line) harmonics of the low energy EPU are shown by the red lines. The other solid lines correspond to the first, third, fifth, and seventh harmonic values for the high-energy IVU, **b** the beam divergence depends on the energy (4σ apertures were adopted for all unmarked lines)

considered in the design of our beamline. To block the Bremsstrahlung radiation induced by SM1, an iron tungsten nickel alloy, of size $H:120 \text{ mm} \times V:120 \text{ mm} \times L:50 \text{ mm}$ was employed as the radiation block material in the safety shutter in the front end. An optical hutch was connected to the front end in both the hard and soft X-ray branches, while all tubes in the optical hutch were wrapped in a lead sheath to prevent the induced SM1 Bremsstrahlung radiation. In this way, the calculated radiation was below $0.5 \mu\text{Sv/h}$ at the exit of the optical hutch in the soft X-ray branch.

The monochromatization of the soft X-ray in the combined beamline was based on a variable line spacing monochromator and an exit slit. Three blazed gratings with central line densities of 300, 800, and 1200 l/mm were

chosen, while the variable included angle was determined using a tilting mirror SM2 in the monochromator, similar to the reported in-focus variable line spacing plane grating monochromator [19]. The grating monochromator focused the beamline to the slit at 41.8 m in the vertical direction, while the plane mirror SM3b deflected the beam to the APPES end station, as indicated by the red solid line in Fig. 2. In the front of the end station, a toroidal mirror (SM7a) was employed to refocus the soft X-ray beam in both the horizontal and vertical directions. The source of the SM7a in the horizontal direction located at 1.317 m was the light source of the soft X-rays. The vertical source originated from the V-slit at 41.8 m. The sample point at 54.6 m was the image of SM7a in both the horizontal and vertical directions.

The hard X-rays in the combined beamline (solid blue line in Fig. 2) were pre-focused in the horizontal direction to the slit at 33 m by a toroidal mirror, HM1, while the beam was parallel aligned in the vertical direction. The source of HM1 in both the horizontal and vertical directions was located at -1.225 m and was the light source of the hard X-rays. A plane grating monochromator (PGM2) or double-crystal monochromator (DCM) were used to monochromatize the incident beam. The two monochromators were placed in series and used separately by slipping the incident beam and referring to the photon energy. The fixed groove density PGM (PGM2, 800 and 1200 l/mm) covered the energy range 1500–2300 eV, while the monochromatic light, with an energy range from 2300 eV–10 keV, was realized by the DCM. The PGM was a Petersen-type monochromator [20], while Si(111) was mainly used as crystal in the DCM; Si(311) crystals are reserved for high-energy resolution experiments. The lattice d-spacing was 0.313 nm for the Si(111) crystal, and the Bragg angle was 23.3° for a beam energy of 5 keV.

A cylindrical mirror HM3 deflected the beam to the combined beamline station, focusing the beam in the vertical direction to the slit at 44.6 m, and the source was located at -1.225 m . In the following, a bended toroidal mirror (HM4a) was employed to refocus the hard X-ray beam. The source of the HM4a in the horizontal direction was located at 33 m and was the H-slit of the combined hard X-rays. The vertical source originated from the V-slit at 44.6 m. The sample point at 54.6 m was the image of HM4a in both the horizontal and vertical directions.

Except for the soft/hard X-ray combined beamline, the individual soft and hard X-ray branches were designed so that the platform with multiple methods could be carried out. In the soft X-ray branch, the photon energy ranged from 130 to 1500 eV, which covered the K-edge of non-metal elements (e.g., B, C, and N) and L-edge of most transition metals (e.g., Fe, Co, Ni, and Mn). A linear translation of the plane mirror from SM3b to SM3a,

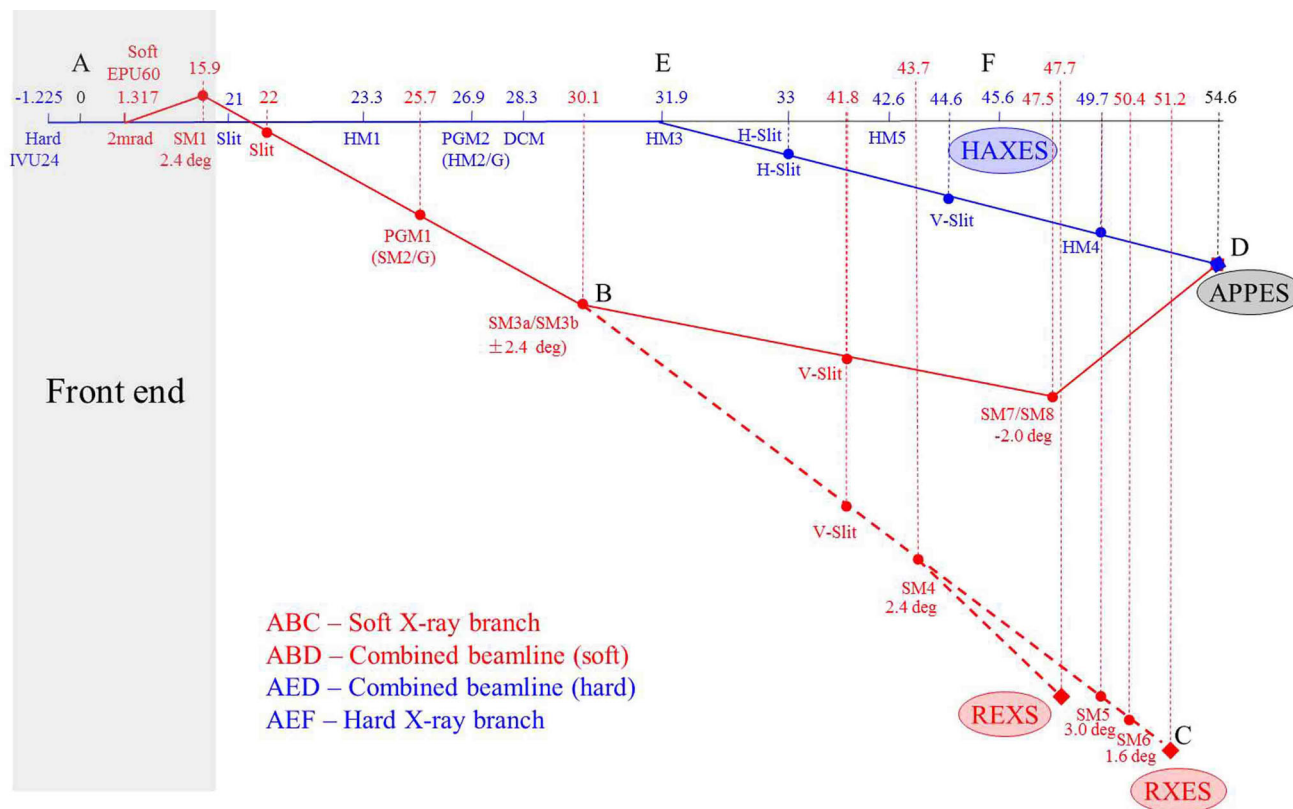


Fig. 2 (Color online) The optical path layout of the E-line. The main optical components of the beamline were plane mirrors (SM1, SM2, SM3a/SM3b, SM7b, HM2, and HM4b), a cylindrical mirror (HM3), elliptical mirrors (SM5 and SM6), toroidal mirrors (SM4, SM7a, HM1, HM4a, and HM5), plane grating monochromators (PGM1 and PGM2), and a double-crystal monochromator (DCM). All incident and deflection mirror angles for the hard X-rays were 3.5 mrad, and

deflected the beam to the soft X-ray branch, as expressed by the red dashed line (Fig. 2). A toroidal mirror, SM4, was designed to capably move in the soft X-ray branch, so that the optical beam could be refocused and deflected out of the storage ring to the REXS station. The source of SM4 in the horizontal direction was located at 1.317 m and was the light source of soft X-ray, and the vertical source originated from the V-slit at 41.8 m. The sample point at 45 m was the image of SM4 in both the horizontal and vertical directions. When the toroidal mirror SM4 was offline, the soft X-ray passed through the REXS chamber directly and was refocused by an elliptical Kirkpatrick–Baez mirror SM5 in the horizontal direction and SM6 in the vertical direction to the inelastic RXES end station at 51.2 m. The sources of SM5 and SM6 in the horizontal direction were 1.317 and 41.8 m (V-slit), respectively.

Meanwhile, by shifting the cylinder mirror HM3 away from the combined hard X-ray beamline, the incident beam reached the hard X-ray branch directly and the refocusing optical mirror, HM5, transported the beam into the HAXES end station at 45.6 m. The source of HM5 in the horizontal

the deflection angles for the soft X-rays are demonstrated in this figure. H-slit and V-slit denote the horizontal and vertical slits, respectively. The paths, components, and distance values marked in red and blue represent the soft and hard branches, respectively. The distance shown on the ruler at the top is measured from the center of the straight section. The areas shaded in gray show the range of the front end

direction was located at 33 m and was the H-slit of the hard X-ray branch. The vertical source originated from the hard X-ray source at -1.225 m. Herein, the hard X-ray branch covered an energy range from 3 to 18 keV modulated by the DCM, so the K-edges of the most frequently used elements were considered.

3.2 Plane mirror in the front end

Due to the complicated experimental platform and compact optical components in the constructed beamline, the plane mirror, SM1, was designed to be located in the front end so that the soft and hard X-rays were separated efficiently. In this way, the components in the beamlines were well arranged in a limited space, and the deflection angle of the optical mirrors (SM3b) could be reduced because of increments in the horizontal space relative to the storage ring, improving the photo flux in the soft X-ray branch end stations. Moreover, the location of SM1 in the front end ensured that the Bremsstrahlung radiation was

within the ring tunnel and eased radiation safety measures in the experimental hall.

Due to the large radiation dose at SM1, a side-cooling solution was chosen instead of internal water cooling because the latter has more potential risk of water leakage caused by degraded glue that binds to the upper plate and bottom block with embedded channels. The key issue of the feasibility was to evaluate the surface error in the side-cooling condition. By applying side water with a speed of 5 l/min, the calculated maximum temperature was 38.7 °C via finite element analysis, which is low enough to maintain the safety of such a plane mirror. The root-mean-square (RMS) value of the thermal deformation was estimated to be 8.95 and 3.97 μrad along the tangential (along the X-ray propagation) and sagittal (perpendicular to the X-ray propagation) directions, respectively, within the spot size range.

Assuming that the thermal deformation of SM1 was 10 and 5 μrad along the tangential and sagittal directions, respectively, the resolving power at the exit slit of the soft X-ray in the combined beamline was kept at 22,182 ($E/\Delta E$) at 244 eV (Fig. 3a, b), indicating a minimal difference ($\sim 9\%$) with an ideal plane mirror, far beyond the required value (15,000 for 244 eV). Moreover, the full width at half maximum (FWHM) of the simulated spot size at the end station of the combined soft X-ray beamline was $H:78 \mu\text{m} \times V:32 \mu\text{m}$ with the assumed surface error, while the simulated spot size was $H:63 \mu\text{m} \times V:32 \mu\text{m}$ in the ideal case. The spot difference in the horizontal direction did not lead to an obvious difference in the APPES analysis for isotropy materials, such as chemical catalysis. The simulated spot sizes are shown in Fig. 3c, d. This suggests that the design of SM1 in the front end with side water cooling does not obviously affect the beam resolution and spot size at the end station, which is a good choice for balancing the limited space, flux performance, and risks.

3.3 Grating monochromator in the combined hard X-ray beamline

The thermal loading carried by the high harmonic was relatively large because the light source was located in the vacuum undulator. The localized power density reached 1.7–1.9 W/mm^2 in the hard X-ray combined beamline, and the calculated surface error of the monochromator was 23 μrad with a water flow of 7 l/min, greatly lowering the energy resolution of the beamline.

As the thermal deformation of silicon crystals induced by heat loads depend on the thermal conductivity and thermal expansion coefficient, liquid-nitrogen-cooled silicon crystals have been successfully used at high heat loads [21, 22]. Heat and surface errors can be effectively reduced by liquid nitrogen cooling [23]. A simulation of the plane

mirror in PGM2 was conducted at 2000 eV under the temperature of liquid nitrogen ($\sim 77 \text{ K}$) with a thermal convection coefficient of $3000 \text{ W}/\text{m}^2 \text{ K}$ [24]. The footprint on the reflection mirror was $H:70 \text{ mm} \times W:5 \text{ mm}$, and the model of the reflection mirror in PGM2 is shown in Fig. 4a. By applying an incident total power of 152.4 W in finite element analysis, the distribution of the temperature with a maximum value of 84 K was obtained (Fig. 4b), low enough to maintain the stability of the plane mirror in PGM2. The stress and deformation of such a plane mirror under cooling by liquid nitrogen is shown in Fig. 4c, d. The calculated maximum surface error was 0.88 μrad , with an RMS value of 0.47 μrad within the spot size range, small enough to meet the requirement of the desired surface error ($< 2 \mu\text{rad}$). Therefore, liquid nitrogen was selected to cool the plane mirror of the grating monochromator in the combined hard X-ray beamline.

3.4 Beam spot overlap in the combined beamline

To maintain the overlap ratio between the soft and hard X-rays, special considerations are involved in this platform. First, all focusing mirrors in the combined beamline, such as the toroidal mirror SM7a in the soft X-ray and the cylindrical mirror HM3/toroidal mirror HM4a in the hard X-ray, were placed vertically with respect to the ground so that the beam spot at the APPES end station would not be far from the center in the vertical direction. Second, two vertically switching toroidal and plane mirrors were placed in the same chamber before the APPES end station; SM7a/SM7b and HM4a/HM4b for the combined soft and hard X-rays, respectively. Herein, the plane mirrors of SM7b and HM4b deflected the large beam spots for both the soft and hard X-rays, respectively, to the end station, producing a general overlap. Finally, a high-resolution monobeam position monitor BPM (e.g., ZnSe) was employed to locate the soft and hard X-ray beam spots accurately by the fluorescence effect with the aid of CCD.

4 Performance

The performance of the beamline was calculated by the Shadow code [25]. The undulator source with 0.01 and 0.1% BW for the soft and hard X-rays, respectively, was employed in the SHADOW calculation. The 4σ aperture ($H:206 \mu\text{rad} \times V:156 \mu\text{rad}$ for 244 eV) in the soft X-ray range and a fixed 3σ ($113 \mu\text{rad} \times 53 \mu\text{rad}$) was adopted in the hard X-ray range to calculate the beam spots, photon flux, and resolving power at the end stations, while the exit slit for the soft X-rays was limited to 30 μm .

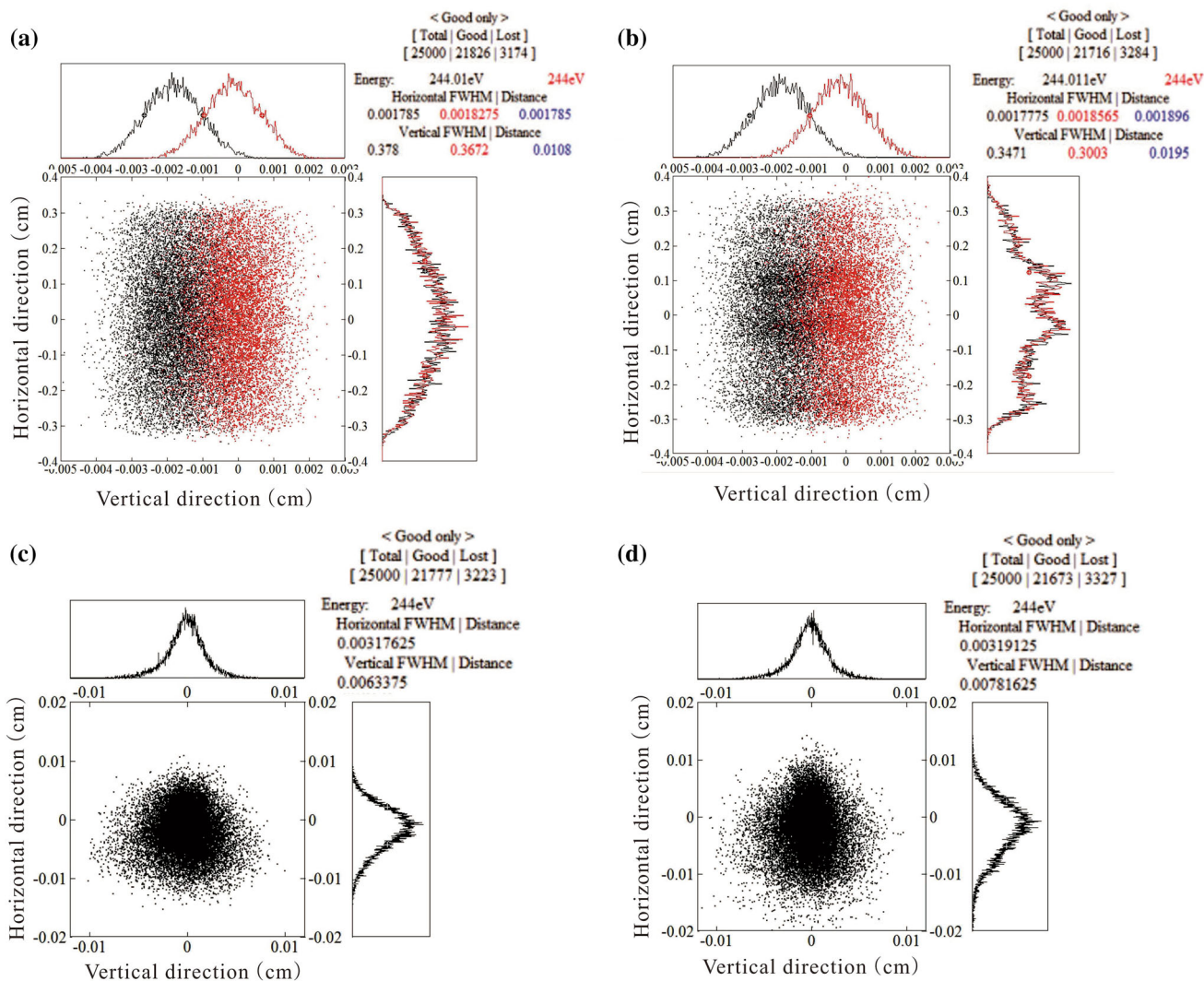


Fig. 3 (Color online) Resolution at the exit slit for the soft X-ray-based combined beamline; **a** for the ideal case of SM1 without surface error and **b** assuming the surface error of SM1 was 10 and 5 μrad along the tangential and sagittal directions, respectively. **c** The simulated beam spot at the soft X-ray-based combined beamline end

station with ideal SM1 and **d** the beam spot when assuming the surface error of SM1 was 10 and 5 μrad along the tangential and sagittal directions, respectively. Herein, the ray tracing employed the Gaussian beam as the light source and its divergence angle was confined by a 4 sigma acceptance angle

4.1 Beam spots at the end stations

In the simulation, the spot sizes at the APPES end station in the combined beamline for both the soft ($H:69.1 \mu\text{m} \times V:36.7 \mu\text{m}$ for 244 eV) and hard ($H:63.0 \mu\text{m} \times V:27.1 \mu\text{m}$ for 2000 eV) X-rays were comparable with a high overlap ratio (Fig. 5a, b), indicating the rationality of the optical path design.

Except for the APPES end station at the combined beamline, the beam spots at inelastic RXES and REXS end stations in the soft X-ray branch are demonstrated in Fig. 6a, b. The observed spot size at the sample point of the inelastic RXES station was $H:17.6 \mu\text{m} \times V:3.5 \mu\text{m}$ with

an exit slit of 30 μm and was small enough to obtain good spectral resolution. On the other hand, the simulated spot size at the REXS was $H:62.2 \mu\text{m} \times V:53.6 \mu\text{m}$ with an exit slit of 30 μm . The calculated divergence angle was 1.92 mrad and was small enough to produce negligible spectrum broadening in the REXS measurement. Moreover, the designed spot size for the HAXES station was $H:68.6 \mu\text{m} \times V:11.0 \mu\text{m}$, as shown in Fig. 6c.

4.2 Resolving power

The resolving power is calculated by $E/\Delta E$, where E is the incident photon energy, ΔE is the beamline resolution

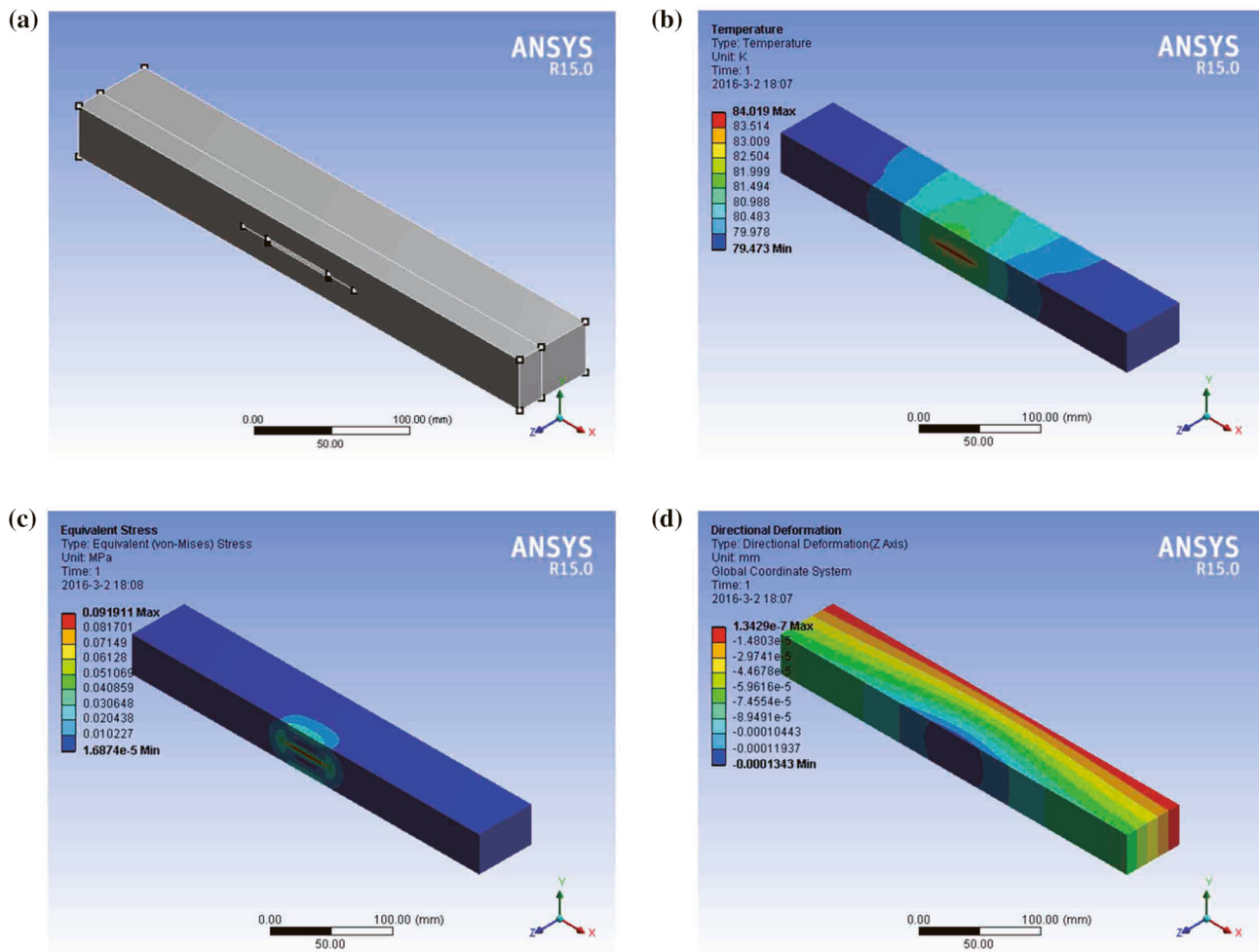


Fig. 4 (Color online) **a** Model of the reflection plane mirror with an Si substrate in PGM2 in the hard X-ray of the combined beamline, **b** the distribution of temperature in the reflection plane mirror, **c** the

stress analysis based on the reflection plane mirror, **d** the deformation of the reflection plane mirror under liquid nitrogen cooling

contributed by the spot-size-limited resolution ΔE_{spot} , ΔE_{diff} is the diffraction-limited resolution, and ΔE_{slit} is the exit slit limited resolution, as expressed by Eq. (1) [26]:

$$\Delta E = \left(\Delta E_{\text{spot}}^2 + \Delta E_{\text{diff}}^2 + \Delta E_{\text{slit}}^2 \right)^{1/2}. \tag{1}$$

Herein, the exit slit limited resolution ΔE_{slit} is determined by the following formula,

$$\Delta E_{\text{slit}} = d \times E^2 \times \cos \beta / (1.24 \times k \times N \times f),$$

where d is the fixed width of exit slit, β is the exit angle at the grating, k is the diffraction order, and f is the exit arm [27].

The resolving power results of the combined soft X-rays are shown in Fig. 7a with an exit slit of 30 μm . The maximum resolving power surpassed 15,000 below 400 eV using a grating line density of 800 l/mm. In detail, the calculation confirmed that a resolving power of 9356 at $h\nu = 244$ eV was achieved with a 300 l/mm grating line

density. Meanwhile, a resolving power of 9809 and 10,167 were achieved with grating line densities of 800 and 1200 l/mm, respectively.

A Gaussian beam source was further employed to confirm the distinguished beam spots for the corresponding resolving power. Ray tracing (Fig. 7b–d) at 244, 900, and 1500 eV (grating line densities of 300, 800, and 1200 l/mm, respectively) demonstrated that beam spots with resolving powers of 9356, 9809 and 10,167, respectively, could be obviously separated at the exit slit.

In the combined hard X-ray beamline, the resolving power as a function of photon energy was calculated (Fig. 8a) for a 30 μm exit slit. Resolving powers of 3710 and 4545 were achieved with 800 and 1200 l/mm grating line densities, respectively, for $h\nu = 2000$ eV. The distinguished beams obtained by the ray tracing simulation using a Gaussian beam source (Fig. 8b) further confirmed that a resolving power of 4545 ($h\nu = 2000$ eV) could be

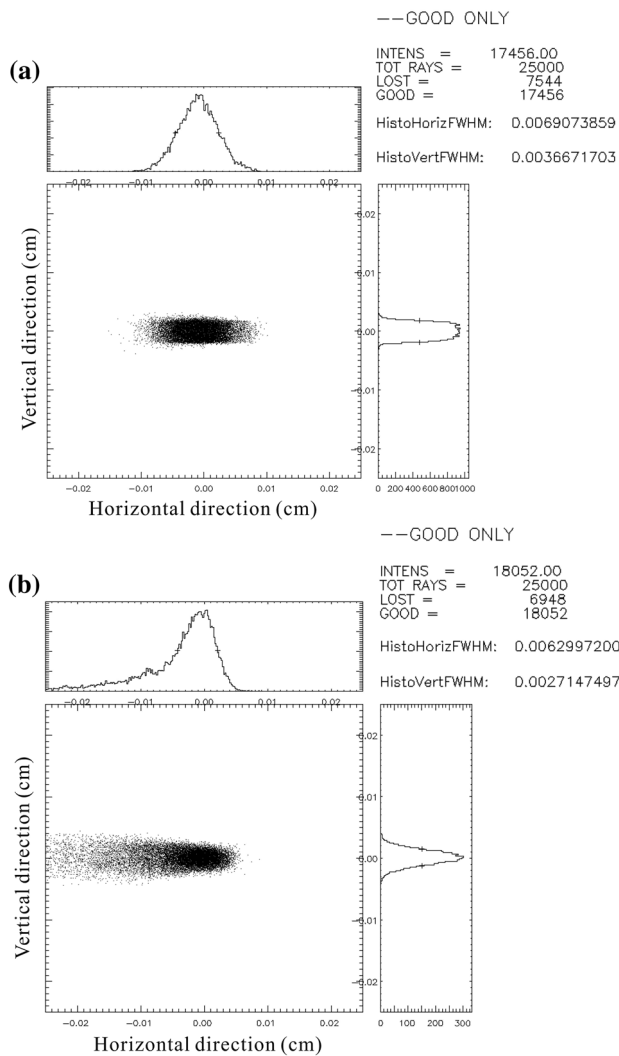


Fig. 5 Simulated beam spot at the APPEs end station produced by **a** soft X-rays of the combined beamline at 244 eV with an FWHM spot size of $H:69.1 \mu\text{m} \times V:36.7 \mu\text{m}$ and **b** hard X-rays of the combined beamline at 2000 eV with an FWHM spot size of $H:63.0 \mu\text{m} \times V:27.1 \mu\text{m}$. Surface errors, including thermal deformation of SM1 and slope error of other mirrors, were considered in the simulations. The ray tracing employed an undulator source with 0.01%BW for the soft X-rays with an exit slit of 30 μm

achieved with a 1200 l/mm grating line density. The resolving power at a high energy of 5000 eV in the combined hard X-ray beamline was calculated to be ~ 7200 ($\Delta E = 0.7$ eV) using a Si(111) crystal in DCM.

4.3 Photon flux

The photon flux calculation was confined by its resolving power (e.g., the exit slit was 30 μm for the soft X-rays). The derived transmission efficiency at the sample position for the soft X-ray in the combined beamline includes the reflectivity of the mirror, the grating optimized efficiency,

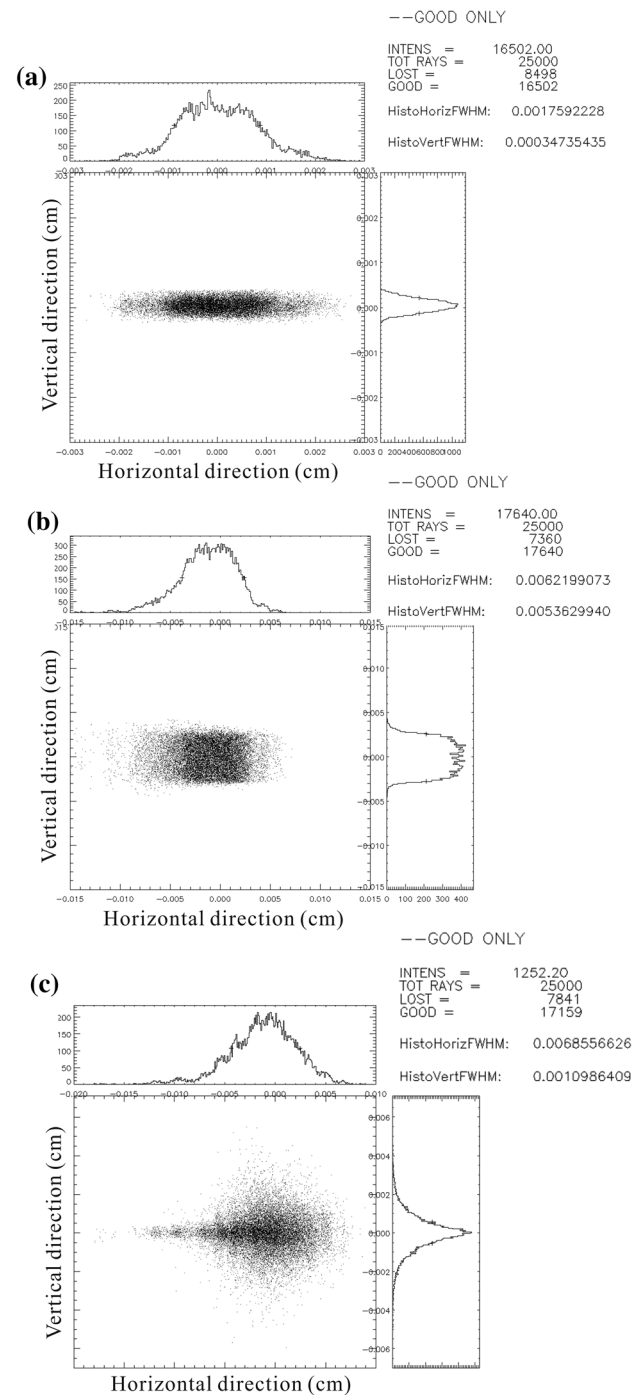


Fig. 6 Simulated beam spot at the **a** inelastic RXES end station for the soft X-rays of the combined branch at 244 eV with a FWHM spot size of $H:17.6 \mu\text{m} \times V:3.5 \mu\text{m}$, **b** REXS end station at 244 eV with a spot size of $H:62.2 \mu\text{m} \times V:53.6 \mu\text{m}$, and **c** hard X-ray HAXES end station of the combined beamline at 5 keV with a spot size of $H:68.6 \mu\text{m} \times V:11.0 \mu\text{m}$. Surface errors including thermal deformations of SM1 and slope errors of other mirrors were considered in simulation. The ray tracing employed an undulator source with 0.01 and 0.1%BW for the soft and hard X-rays, respectively, with a 30 μm exit slit

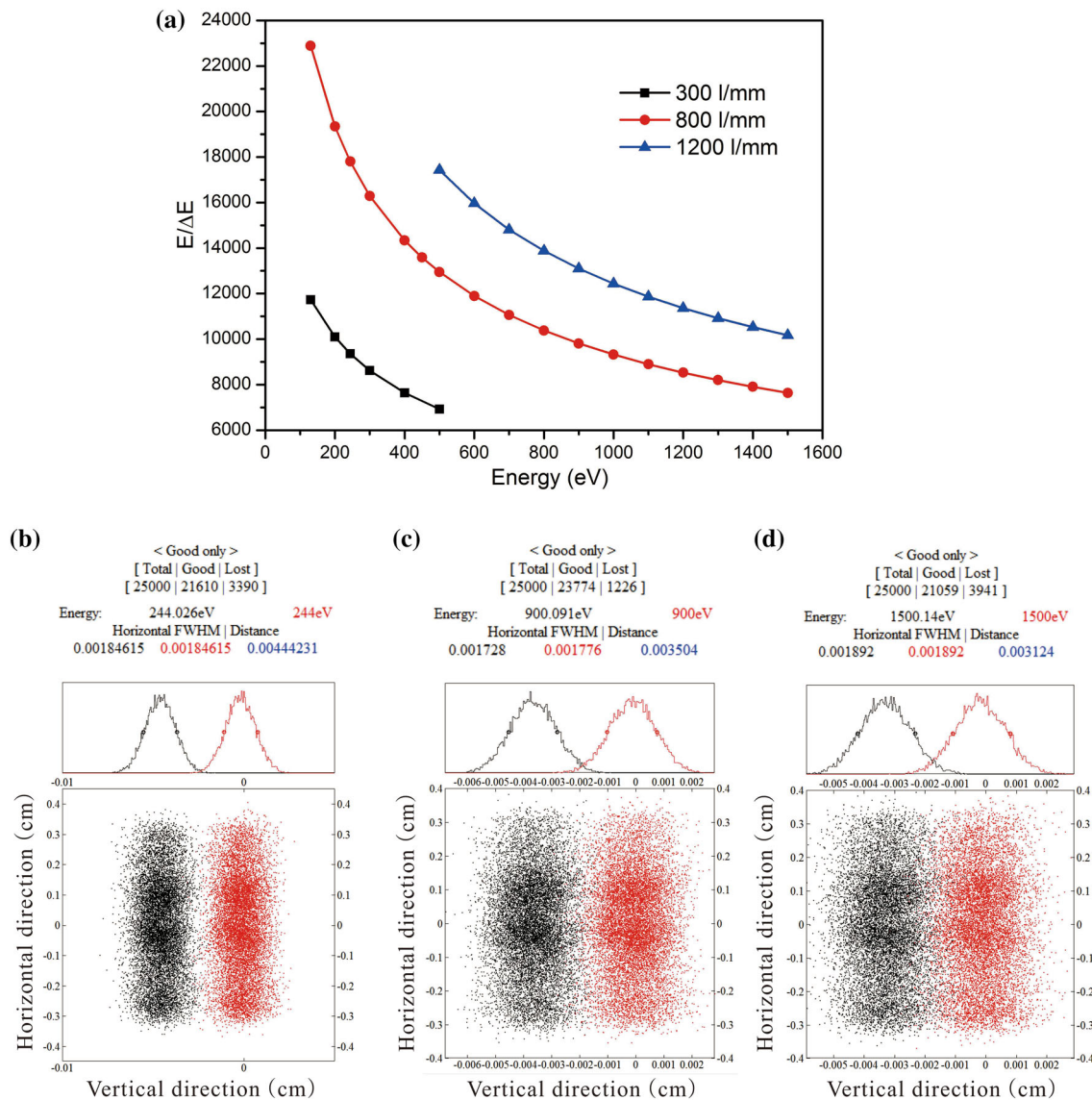


Fig. 7 (Color online) **a** Resolving power ($E/\Delta E$) as a function of photon energy with a 30 μm exit slit. The three lines correspond to the result of three grating line densities (300, 800, and 1200 l/mm). The cosine ratio C_{ff} ($\cos\beta/\cos\alpha$, where α and β are the incident and reflection grazing angle of gratings, respectively) was assumed to be 2, 2.6, and 3.65 for gratings with line densities of 300, 800, and 1200 l/mm, respectively. The ray tracing (with slope error) using a

Gaussian beam source showed two distinguished spots for the combined soft X-ray beamlines at **a** $h\nu = 244$ eV, **b** $h\nu = 900$ eV, and **c** $h\nu = 1500$ eV, with grating groove densities of 300 l/mm, 800 and 1200 l/mm, respectively. Surface errors, including thermal deformation of SM1 and slope errors of the other mirrors, were considered in the simulations

and the surface roughness of the optics, as shown in Table S1a (Supporting information). The flux at the end station was estimated by multiplying the flux of the undulator (Fig. 1a) with the transmission efficiency of each mirror and efficiency of monochromators (Fig. S1a, S1c). The flux of the undulator was calculated from the SPECTRA code [18], and the transmission efficiencies of the mirrors were obtained from the XOP software [28]. The theoretical flux at the APPES end station reached 10^{12} phs/s with an exit slit of 30 μm in the energy range 130–1500 eV (Fig. 9a) and 2.6×10^{12} phs/s with a

resolving power of 9356 (exit slit 30 μm) at 244 eV in the combined soft X-ray beamline with a grating line density of 300 l/mm.

Compared with the soft X-ray combined beamline, the soft X-ray branch was designed with one more mirror (Table S1b), so the flux at the final inelastic RXES station was approximately 22% lower than that at the combined soft X-ray beamline. The theoretical flux in the soft X-ray branch end station (inelastic RXES) was estimated to be 2.0×10^{12} phs/s with a resolving power of 9356 (exit slit 30 μm) at 244 eV with a grating line density of 300 l/mm.

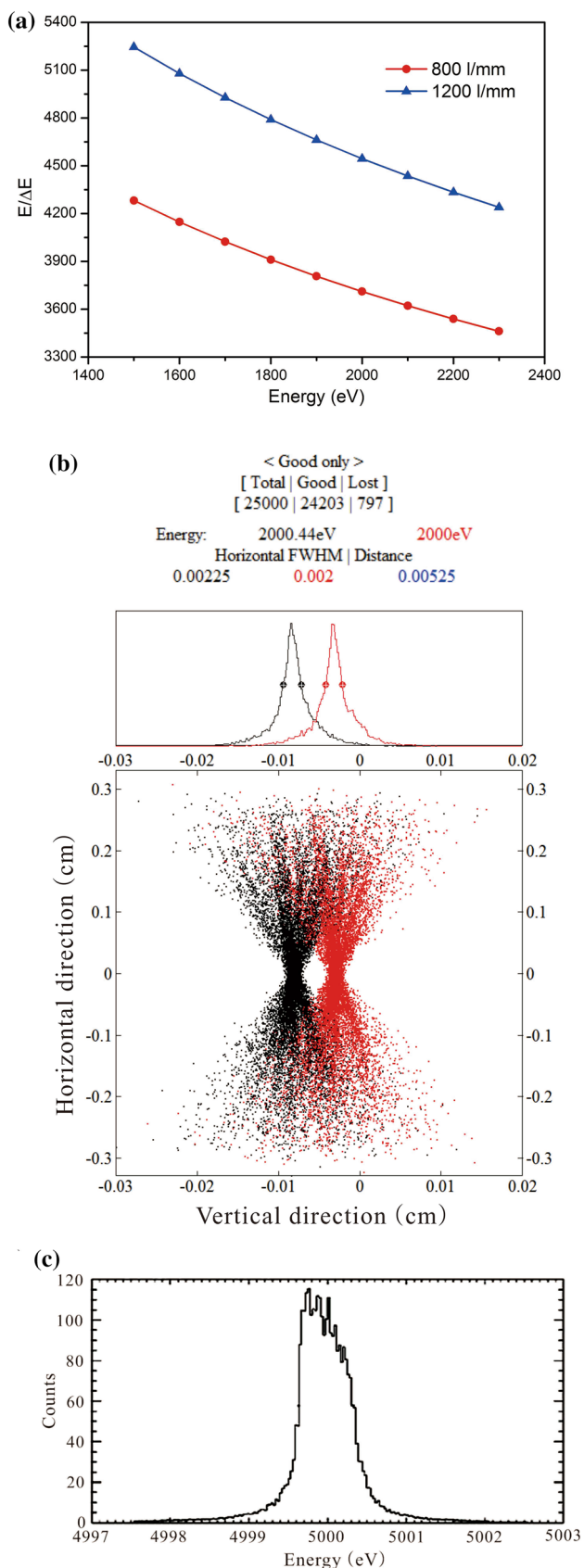


Fig. 8 (Color online) **a** Resolving power as a function of photon energy with an exit slit of $30\ \mu\text{m}$. The two lines correspond to the gratings with line densities of 800 and 1200 l/mm. The C_{fr} was 3.0 for both gratings, **b** the ray tracing (with slope error) using a Gaussian beam source shows two distinguished spots for the combined hard X-ray beamline (2000 eV) with a grating groove density of 1200 l/mm, **c** photon counts as a function of photon energy using a 0.1% BW undulator source at $h\nu = 5000$ eV, and the DCM with a Si(111) crystal was used to produce white beam monochromatization

Similarly, the derived transmission efficiency at the sample position for the PGM2-based hard X-ray (1500–2300 eV) in the combined beamline is shown in Table S2a. All mirrors were coated by a parallel Rh/Cr layer with a desired surface roughness smaller than 0.3 nm. The flux at the APPES end station was greater than 5×10^{11} phs/s with an exit slit of $30\ \mu\text{m}$ in the energy range 1500–2300 eV (Fig. 9b), while it was 2.2×10^{12} phs/s with a resolving power of 3710 (exit slit $30\ \mu\text{m}$) at 2 keV in the hard X-ray-based combined beamline for a grating line density of 800 l/mm.

The transmission efficiency at the sample position for the DCM-based hard X-ray (2300 eV–10 keV) in the combined beamline is shown in Table S2b. The flux at the APPES end station was 5×10^{12} phs/s in the energy range 2300 eV–10 keV (Fig. 9c), while it was 1.8×10^{13} phs/s with a resolving power of 7200 at 5 keV in the hard X-ray-based combined beamline for monochromatization by DCM.

The hard X-ray branch was designed with one less mirror (Table S2c), and the flux at the HAXES station was $\sim 10\%$ higher than that at the combined hard X-ray beamline by DCM. The theoretical flux at the hard X-ray branch end station was estimated to be 1.98×10^{13} phs/s with a resolving power of 7200 at 5 keV.

5 Summary

In this report, a new wide-energy-range beamline with a multifunctional experiment platform was designed at the SSRF. Two canted undulators were used to realize a wide-range analysis by X-rays, applicable to the study of properties of various energy materials, benefiting their development. In the optical path, the plane mirror SM1 was placed in the front end with side water cooling to balance the limited space, flux performance, and risks. The plane mirror in PGM was cooled by liquid nitrogen in the combined hard X-ray beamline to reduce the surface error below $2\ \mu\text{rad}$. By simulation with the shadow code, the combined beamline achieved a theoretical photon flux $> 10^{12}$ phs/s with a $30\ \mu\text{m}$ exit slit in soft X-ray and

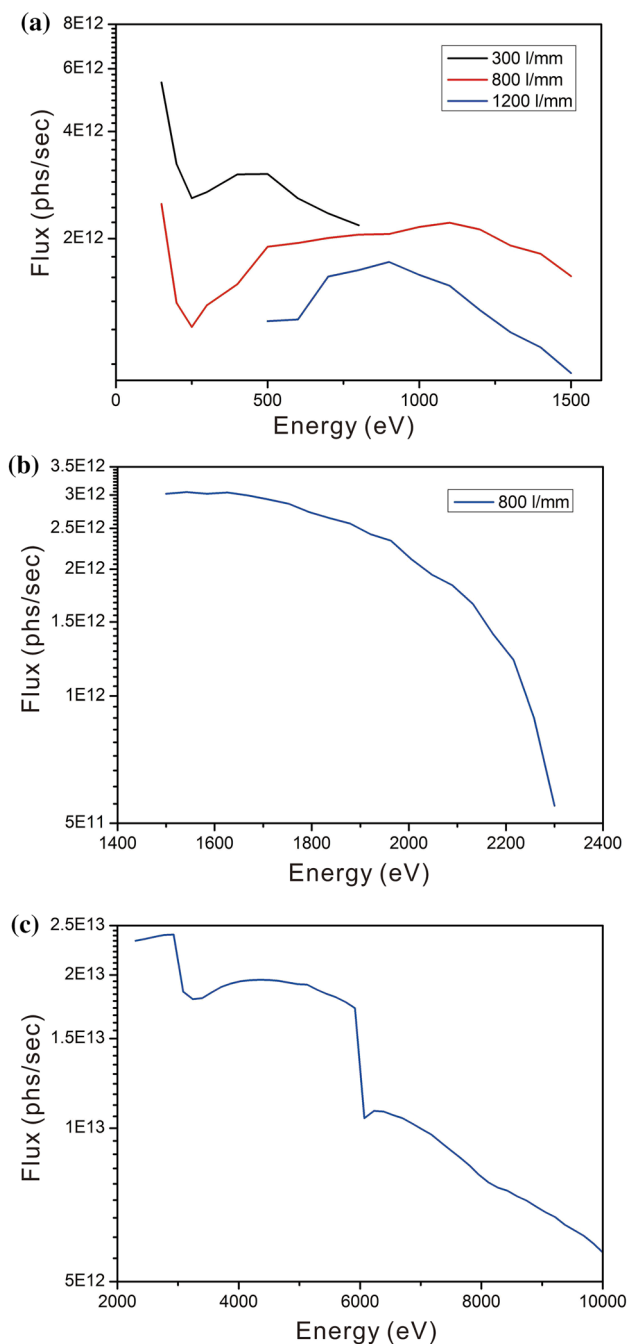


Fig. 9 (Color online) **a** Photo flux at the combined soft X-ray APPES end station in the energy range 130–1500 eV, with three frequently used grating line densities of 300, 800, and 1200 l/mm. **b** Photo flux at the combined hard X-ray APPES end station in the energy range 1500–2300 eV, with a frequently used grating line density of 800 l/mm (both 800 and 1200 l/mm covered the whole energy range; thus, 1200 l/mm is not shown), **c** photo flux at the combined hard X-ray APPES end station in the energy range 2300–10 keV with monochromatization by DCM. 0.1%BW was selected for both the soft and hard X-ray flux calculations

$> 5 \times 10^{12}$ phs/s in hard X-ray within 0.1%BW. The maximum resolving powers were $> 15,000$ and > 6000 in the soft and hard X-rays, respectively.

Acknowledgements This work is supported by the National Science Foundation of China (Grant No. 11505280, 11475251, 11225527), the Shanghai Youth Foundation (Grant No. 14YF1407500), the National Development and Reform Commission (NDRC) of China. We also thank the engineers and staff in SSRF for valuable discussion.

References

1. R. Noyori, Synthesizing our future. *Nat. Chem.* **1**, 5–6 (2009). <https://doi.org/10.1038/nchem.143>
2. M. Lang, F. Zhang, J. Zhang et al., Nanoscale manipulation of the properties of solids at high pressure with relativistic heavy ions. *Nat. Mater.* **8**, 793–797 (2009). <https://doi.org/10.1038/nmat2528>
3. P. Liu, Y. Zhao, R. Qin et al., Photochemical route for synthesizing atomically dispersed palladium catalysts. *Science* **352**(6287), 797–801 (2016). <https://doi.org/10.1126/science.aaf5251>
4. B. Zhang, X. Zheng, O. Voznyy et al., Homogeneously dispersed, multimetal oxygen-evolving catalysts. *Science* **352**(6283), 333–337 (2016). <https://doi.org/10.1126/science.aaf1525>
5. R. Mu, Q. Fu, H. Xu et al., Synergetic effect of surface and subsurface Ni species at Pt–Ni bimetallic catalysts for CO oxidation. *J. Am. Chem. Soc.* **133**(6), 1978–1986 (2011). <https://doi.org/10.1021/ja109483a>
6. J. Liu, Q. Zhao, J.L. Liu et al., Heterovalent-doping-enabled efficient dopant luminescence and controllable electronic impurity via a new strategy of preparing II–VI nanocrystals. *Adv. Mater.* **27**, 2753–2761 (2015). <https://doi.org/10.1002/adma.201500247>
7. R. Lindblad, D. Bi, B. Park et al., Electronic structure of TiO₂/CH₃NH₃PbI₃ perovskite solar cell interfaces. *J. Phys. Chem. Lett.* **5**, 648–653 (2014). <https://doi.org/10.1021/jz402749f>
8. Z.H. Chen, W.Q. Peng, K. Zhang et al., Band alignment by ternary crystalline potential-tuning interlayer for efficient electron injection in quantum dot-sensitized solar cells. *J. Mater. Chem. A*. **2**, 7004–7014 (2014). <https://doi.org/10.1039/C3TA15435A>
9. R.T. Vang, E. Lægsgaard, F. Besenbacher, Bridging the pressure gap in model systems for heterogeneous catalysis with high-pressure scanning tunneling microscopy. *Phys. Chem. Chem. Phys.* **9**, 3460–3469 (2007). <https://doi.org/10.1039/B703328C>
10. W.X. Huang, Oxide nanocrystal model catalysts. *Acc. Chem. Res.* **49**(3), 520–527 (2016). <https://doi.org/10.1021/acs.accounts.5b00537>
11. Y. Ren, High-energy synchrotron X-ray diffraction and its application to in situ structural phase-transition studies in complex sample environments. *JOM* **64**(1), 140–149 (2012). <https://doi.org/10.1007/s11837-011-0218-8>
12. L. Luo, S. Zhang, Applications of synchrotron-based X-ray techniques in environmental science. *Sci. China. Chem.* **53**(12), 2529–2538 (2010). <https://doi.org/10.1007/s11426-010-4085-x>
13. J. Rundgren, Electron inelastic mean free path, electron attenuation length, and low-energy electron-diffraction theory. *Phys. Rev. B*. **59**(7), 5106–5114 (1999). <https://doi.org/10.1103/PhysRevB.59.5106>
14. M. Wimmer, M. Bär, D. Gerlach et al., Hard X-ray photoelectron spectroscopy study of the buried Si/ZnO thin-film solar cell interface: direct evidence for the formation of Si–O at the expense of Zn–O bonds. *Appl. Phys. Lett.* **99**(152104), 1–3 (2011). <https://doi.org/10.1063/1.3644084>
15. G. Materlik, T. Rayment, D.I. Stuart, Diamond light source: status and perspectives. *Philos. Trans. A. Math. Phys. Eng. Sci.* **373**(2036), 1–16 (2015). <https://doi.org/10.1098/rsta.2013.0161>

16. R. Reininger, J.C. Woicik, S.L. Hulbert et al., NIST NSLS-II spectroscopy beamline optical plan for soft and tender X-ray spectroscopy and microscopy (100 eV to 7.5 keV). *Nucl. Instrum. Methods Phys. Res. Sect. A* **649**, 49–51 (2011). <https://doi.org/10.1016/j.nima.2010.11.172>
17. R. Follath, M. Hvecker, G. Reichardt et al., The energy materials in situ laboratory berlin (EMIL) at BESSY II. *J. Phys. Conf. Ser.* **425**, 212003 (2003). <https://doi.org/10.1088/1742-6596/425/21/2122003>
18. T. Tanaka, H. Kitamura, SPECTRA: a synchrotron radiation calculation code. *J. Synchrotron Rad.* **8**, 1221–1228 (2001). <https://doi.org/10.1107/S090904950101425X>
19. R. Reininger, The in-focus variable line spacing plane grating monochromator. *Nucl. Instrum. Methods Phys. Res. Sect. A* **649**, 139–143 (2011). <https://doi.org/10.1016/j.nima.2010.12.162>
20. S.I. Fedoseenko, D.V. Vyalikh, I.E. Iossifov et al., Commissioning results and performance of the high-resolution Russian–German Beamline at BESSY II. *Nucl. Instrum. Methods Phys. Res. Sect. A* **505**, 718–728 (2003). [https://doi.org/10.1016/S0168-9002\(03\)00624-7](https://doi.org/10.1016/S0168-9002(03)00624-7)
21. G. Marot, M. Rossat, A. Freund et al., Cryogenic cooling of monochromators. *Rev. Sci. Instrum.* **63**, 477–480 (1992). <https://doi.org/10.1063/1.1142736>
22. D.H. Bilderback, A.K. Freund, G.S. Knapp, The historical development of cryogenically cooled monochromators for third-generation synchrotron radiation sources. *J. Synchrotron Radiat.* **7**(2), 53–60 (2000). <https://doi.org/10.1107/S0909049500000650>
23. L. Zhang, W.K. Lee, M. Wulff, The performance of a cryogenically cooled monochromator for an in-vacuum undulator beamline. *J. Synchrotron Radiat.* **10**(4), 313–319 (2003). <https://doi.org/10.1107/S0909049503012135>
24. L. Zhang, W.K. Lee, M. Wulff et al., Performance prediction of cryogenically cooled silicon crystal monochromator, in *AIP Conference Proceedings*, vol. 705 (2004), p. 623–626. <https://doi.org/10.1063/1.1757873>
25. B. Lai, F. Cerrina, SHADOW: a synchrotron radiation ray tracing program. *Nucl. Instrum. Methods Phys. Res. Sect. A* **246**, 337–341 (1986). [https://doi.org/10.1016/0168-9002\(86\)90101-4](https://doi.org/10.1016/0168-9002(86)90101-4)
26. V.N. Strocov, T. Schmitt, U. Flechsig et al., High-resolution soft X-ray beamline ADDRESS at the Swiss Light Source for resonant inelastic X-ray scattering and angle-resolved photoelectron spectroscopies. *J. Synchrotron Radiat.* **17**, 631–643 (2010). <https://doi.org/10.1107/S0909049510019862>
27. J.B. West, H.A. Padmore, Optical engineering, in *Handbook on Synchrotron Radiation*, vol. 2, ed. by G.V. Marr (Elsevier, Amsterdam, 1987)
28. S. Rio, R.J. Dejus, XOP: recent developments, in *Proceedings of the SPIE 3448, Crystal and Multilayer Optics* (1998), p. 340. <https://doi.org/10.1117/12.332522>